Single-Atom and Bimetallic Nanoalloy Supported on Nanotubes as a Bifunctional Electrocatalyst for Ultrahigh-Current-Density Overall Water Splitting

Wenhui Luo,[||] Yang Wang,[||] Liuxiong Luo, Shen Gong,* Mengni Wei, Yixuan Li, Xueping Gan,* Yuyuan Zhao, Zhenghong Zhu, and Zhou Li*

ACCESS | 📊 Metrics & More | 📰 Article Recommendations | 🔵ℹ️ Supporting Information

ABSTRACT: Developing exceedingly efficient, cost-effective, and environmentally friendly bifunctional catalysts for the hydrogen evolution reaction (HER) and oxygen evolution reaction (OER) especially at high current density is crucial for realizing the industrial application of electrocatalytic overall water splitting. In this work, non-noble-metal bifunctional catalysts with single Ni atoms, single Fe atoms, and NiFe nanoalloys supported on carbon nanotubes ($Ni_{SA}Fe_{SA}$-Ni_xFe/CNT) are rationally designed and fabricated. In 1 M KOH, the optimized $Ni_{SA}Fe_{SA}$-$Ni_{50}Fe$/CNT catalyst affords low overpotentials of 64 and 227 mV at 10 mA cm^{-2} for catalyzing the HER and OER, respectively. Moreover, the catalyst enables the overall water splitting at a low cell voltage of 1.49 V to achieve 10 mA cm^{-2} in 1 M KOH. At a cell voltage of 1.80 V, the current density is as high as 382 mA cm^{-2}, which surpasses those of most materials reported so far. After a simple two-step oxidation and rereduction procedure, the catalytic performances of the OER, HER, and overall water splitting recover completely to their original levels. This work not only provides a potential catalyst candidate for economically realizing water splitting but also shows a method for reactivatable catalyst design.

KEYWORDS: bifunctional electrocatalyst, single atom, bimetallic nanoalloy, oxygen evolution reaction, hydrogen evolution reaction, overall water splitting
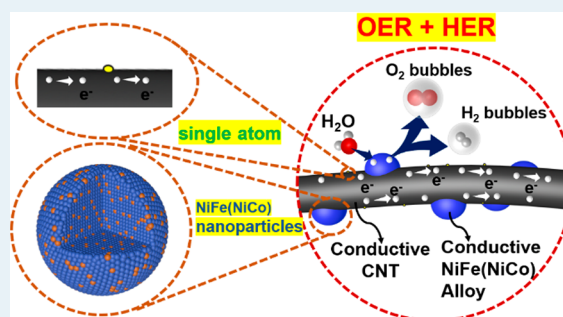
E lectrochemical water splitting has been widely regarded as a very important reaction, because its products, H$_2$ and O$_2$, are closely related to human manufacturing and life.[1−3] H$_2$ produced by the hydrogen evolution reaction (HER) on the cathode is the cleanest energy, and O$_2$, the product of the oxygen evolution reaction (OER) on the anode, is an important raw material for the respiration of living things on the earth.[4] Due to the high energy barrier, especially under the high current density in industrial production, it is necessary to use a catalyst to reduce the required energy and improve energy conversion efficiency.[5,6] OER catalysts usually do not have HER catalytic activity, and vice versa. In the process of electrocatalytic water splitting, different catalysts are usually placed in the same electrolyzer, which will inevitably cause cross-contamination and affect the stability of the reaction.[7] For example, on the basis of previous research, a Pt catalyst can be poisoned by some anions (such as halides, sulfates, and others).[8] Therefore, it is recommended to develop bifunctional catalysts for the HER and OER. For example, Yin et al. recently prepared IrNi-FeNi$_3$ composite materials, in which an IrNi alloy was the active center of the OER reaction, and FeNi$_3$ provided HER catalytic activity. Although IrNi-FeNi$_3$ has excellent catalytic properties, including OER, HER and water

splitting performances, the preparation cost of this catalyst is high because it contains the noble metal Ir. The scarcity and high price of noble metals severely hinders this technology from being widely adopted. It is of great significance to develop exceedingly efficient non-noble-metal overall water splitting catalysts with bicatalytic functions, especially at high current density.[9]

Among various non-noble-metal materials, due to their excellent catalytic properties, Ni-based, Fe-based, and Co-based materials have attracted more and more attention.[10−15] According to previous studies, NiFe and NiCo layered double (oxy)hydroxides will be generated in situ on the surface of NiFe and NiCo alloys as the OER reaction progresses in alkaline electrolytes, which show excellent OER catalytic performance and even surpass those of commercial OER
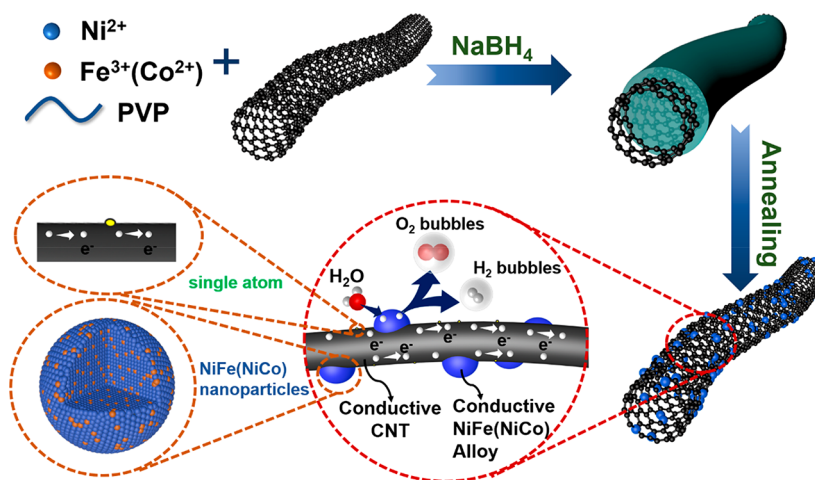
Figure 1. Schematic diagram of the preparation process, electrocatalytic function, and hyperfine microstructure of $Ni_{SA}Fe_{SA}-Ni_xFe/CNT$ and $Ni_{SA}Co_{SA}-Ni_xCo/CNT$.

catalysts such as RuO_2 and IrO_2.[16] Ni-based bimetallic materials (including NiFe and NiCo nanoalloys) and transition-metal-based single-atom materials (including single Ni atoms, single Fe atoms, single Co atoms, and so on) are also used as HER catalysts.[17,18] Herein, two series of non-noble-metal bifunctional catalysts ($Ni_{SA}Fe_{SA}-Ni_xFe/CNT$ and $Ni_{SA}Co_{SA}-Ni_xCo/CNT$) are fabricated, in which single atoms and nanoalloys are simultaneously supported on carbon nanotubes (CNTs).

The system composed of Ni-based bimetallic materials and single atoms that are both supported on CNT has many advantages for OER and HER catalysis. (1) The doping of Fe and Co can enhance the adsorption/desorption capacity of the intermediate products and exert a synergistic effect between the two metals, thus improving the catalytic activity.[19,20] (2) Due to the nanoscale confinement effect, the NiFe (oxy)-hydroxides and NiCo (oxy)hydroxides generated on the surface of NiFe and NiCo nanoalloys are extremely thin (1–5 nm), which neither hinder the migration of electrons in the OER process nor affect the adsorption/desorption of the intermediate products on NiFe and NiCo alloys in the catalytic process.[21,22] In addition, NiFe and NiCo alloys have high conductivity, which are beneficial for efficient electron transfer in catalytic processes. (3) A CNT as the support of these composite catalysts, which is a good electric conductor, can avoid the agglomeration of nanoparticles. In addition, the pores in the nondense packed structure formed by the overlap between CNTs can be the emission channels for gases generated in the catalysis process. As a result, this simultaneously enhances the mass and electron transfer ability of the catalysts.[23]

The $Ni_{SA}Fe_{SA}-Ni_xFe/CNT$ and $Ni_{SA}Co_{SA}-Ni_xCo/CNT$ bifunctional catalysts with adjustable Ni/Fe and Ni/Co ratios prepared in this paper show excellent catalytic performances in the OER, HER, and water splitting. The OER overpotential of the optimized $Ni_{SA}Fe_{SA}-Ni_{50}Fe/CNT$ to reach 10 mA cm^{-2} is only 227 mV with a small Tafel slope of 41.8 mV dec^{-1} and outstanding stability for over 65 h at 10 mA cm^{-2}. It is one of the catalysts with the lowest OER overpotential and the longest OER stability time among the materials reported so far.[24–26] At the same time, $Ni_{SA}Fe_{SA}-Ni_{50}Fe/CNT$ also shows a low HER overpotential of 64 mV to reach 10 mA cm^{-2}, which is competitive with Pt/C, and an outstanding durability for

over 72 h at 10 mA cm^{-2}. A water electrolyzer was assembled with $Ni_{SA}Fe_{SA}-Ni_{50}Fe/CNT$ as both the cathode and anode, and the overpotentials of $Ni_{SA}Fe_{SA}-Ni_{50}Fe/CNT^{(+,-)}$ (+,− means that the same catalyst is used as both a cathode and an anode for water splitting) at 10 and 100 mA cm^{-2} are 260 and 410 mV, respectively. It demonstrates an ultrahigh current density of 382 mA cm^{-2} at a cell voltage of 1.80 V and can be stable for 30 h at 10 mA cm^{-2}. The industrial-grade current density and good durability of $Ni_{SA}Fe_{SA}-Ni_{50}Fe/CNT^{(+,-)}$ for electrocatalytic water splitting surpass those of most materials reported so far and meet the overpotential and current density requirements of industrial catalysts. The mechanism of catalytic activity has been identified by electrochemical tesst, X-ray diffraction (XRD), X-ray photoelectron spectrometry (XPS), scanning electron microscopy (SEM), transmission electron microscopy (TEM), and density functional theory (DFT).

■ RESULTS AND DISCUSSION

In Figure 1, the preparation process, electrocatalytic function for overall water splitting, and the hyperfine microstructure of $Ni_{SA}Fe_{SA}-Ni_xFe/CNT$ and $Ni_{SA}Co_{SA}-Ni_xCo/CNT$ are illustrated. Specifically, a low concentration of sodium borohydride ($NaBH_4$) is first used to create a reductive environment, so that Ni^{2+}, Fe^{3+} (or Co^{2+}), and PVP will form small and dense nucleation sites at the defects on the acid-treated CNT. As shown in Figure S1, the precursors obtained after the reaction in the liquid phase are wrapped on the CNT tube wall. Subsequently, the precursors/CNT are kept at 400 °C in a hydrogen−argon mixed atmosphere for 2 h to prepare the final catalysts. This strategy combined chemical reduction and heat treatment successfully prepare $Ni_{SA}Fe_{SA}-Ni_xFe/CNT$ and $Ni_{SA}Co_{SA}-Ni_xCo/CNT$ composite materials in which fine and uniform alloy nanoparticles with a high surface-coating rate and abundant single atoms coexist on CNT. These obtained composite materials containing multiple catalytic sites for the OER and HER demonstrate excellent electrocatalytic activity for overall water splitting. Moreover, the heterostructure is noteworthy in that these highly conductive catalysts with an alloy core and CNT support can provide more channels for electron migration and then increase the rate of electron migration.[27] The two series $Ni_{SA}Fe_{SA}-Ni_xFe/CNT$ and $Ni_{SA}Co_{SA}-Ni_xCo/CNT$ are prepared by changing the concen-
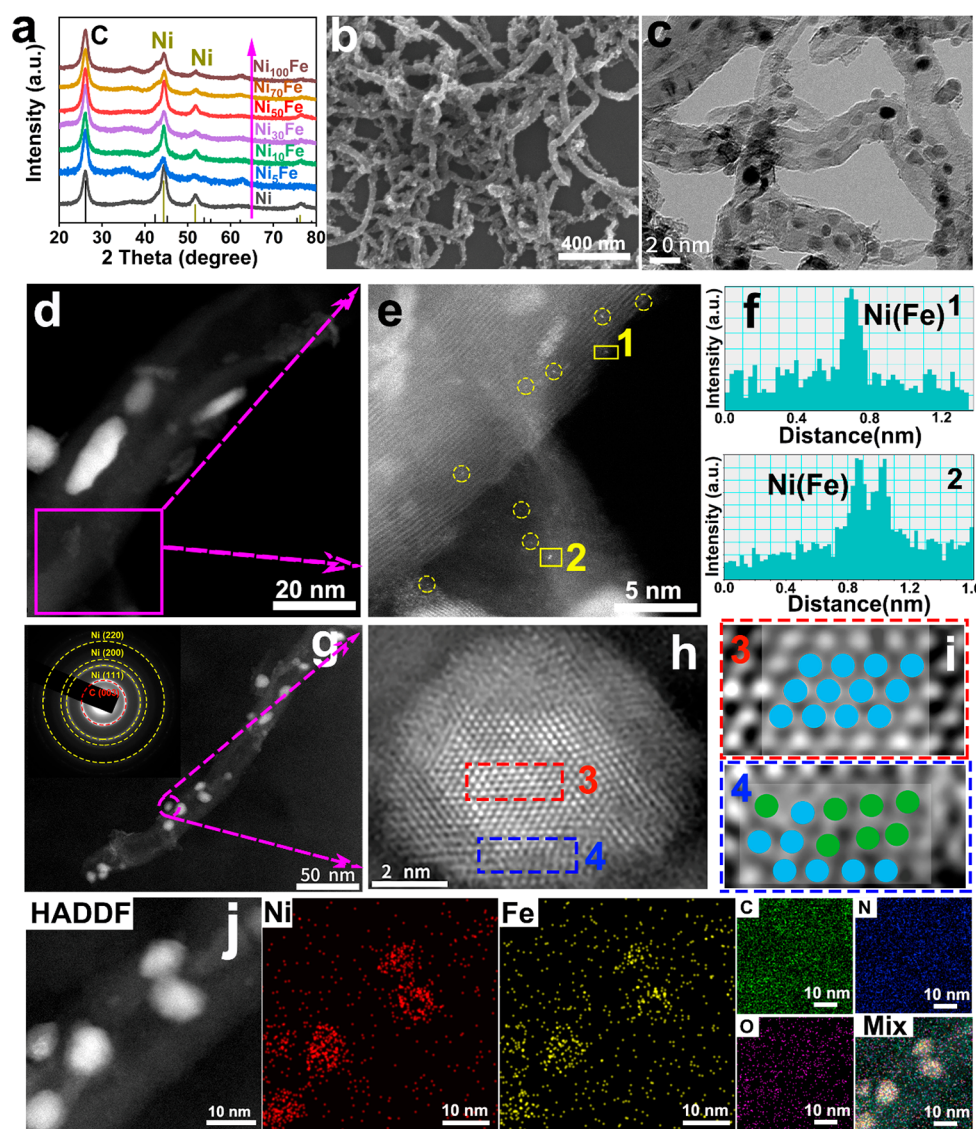
Figure 2. Phase of $Ni_{SA}Fe_{SA}-Ni_xFe/CNT$ and the morphology, microstructure, and elemental composition of $Ni_{SA}Fe_{SA}-Ni_{50}Fe/CNT$. (a) XRD diffraction patterns of $Ni_{SA}Fe_{SA}-Ni_xFe/CNT$ (x = 0, 5, 10, 30, 50, 70 100). (b−d) SEM, TEM, and STEM images of $Ni_{SA}Fe_{SA}-Ni_{50}Fe/CNT$, respectively. (e) High-resolution HAADF-STEM images, where the bright spots marked by the yellow circles and rectangles represent single Ni atoms and single Fe atoms, respectively. (f) Linear scanning analysis of single atoms remarked by yellow rectangles in (e). (g) STEM image of $Ni_{SA}Fe_{SA}-Ni_{50}Fe/CNT$. The inset is the selected area electron diffraction. (h) Z-contrast image of $Ni_{SA}Fe_{SA}-Ni_{50}Fe/CNT$. (i) Magnified views of the selected areas in the red rectangle (position 3) and blue rectangle (position 4) in (h) (the blue balls represent ordered atoms, and the green balls represent chaotic atoms). (j) HADDF-STEM and EDS element mapping of Ni, Fe, and C elements in $Ni_{SA}Fe_{SA}-Ni_{50}Fe/CNT$.

tration ratio of metal ions to optimize the catalytic performance. The catalysts are named according to the molar concentration ratio of different ions in the added metal salt solution. For example, if the Ni^{2+}/Fe^{3+} molar concentration ratio is equal to 50/1 in the salt solution, it is named $Ni_{SA}Fe_{SA}-Ni_{50}Fe/CNT$.

The phases of $Ni_{SA}Fe_{SA}-Ni_xFe/CNT$ and $Ni_{SA}Co_{SA}-Ni_xCo/CNT$ have been identified by XRD, and the results are shown in Figure 2a and Figure S2, respectively ($Ni_{SA}Fe_{SA}-Ni_xFe/CNT$ is abbreviated as Ni_xFe in Figure 2a: for example, $Ni_{SA}Fe_{SA}-Ni_{50}Fe/CNT$ is abbreviated as $Ni_{50}Fe$). It is well-known that there are no obvious diffraction peaks for single atoms; therefore, the XRD patterns of $Ni_{SA}Fe_{SA}-Ni_xFe/CNT$ and $Ni_{SA}Co_{SA}-Ni_xCo/CNT$ are only matched with those of carbon and Ni metal. The wide diffraction peak at $2\theta \approx 26°$ is consistent with the (003) crystal plane of graphene (PDF #01-

073-5918), indicating that the graphitization degree of CNT increases after the acid treatment. The diffraction peaks at 2θ = 44.7, 52.1, and 76.8° correspond to the (111), (200), and (220) crystal planes of metallic nickel (PDF #04-006-6387), respectively. It is notable that the substitution of Fe for Ni does not change the crystal structure and crystal plane spacing because of the similarity of atomic radii between Ni and Fe.[28] As a result, the diffraction peaks of $Ni_{SA}Fe_{SA}-Ni_xFe/CNT$ and $Ni_{SA}Co_{SA}-Ni_xCo/CNT$ doped with different proportions of Fe and Co are almost the same as those of Ni/CNT. SEM and TEM are applied to confirm the microstructure of $Ni_{SA}Fe_{SA}-Ni_xFe/CNT$ and $Ni_{SA}Co_{SA}-Ni_xCo/CNT$. In comparison with the acid-treated CNT (Figure S3a), many fine nanoparticles are formed on the surface of the CNT after heat treatment (Figure 2b,c and Figures S3c,d and S4−S8). The morphologies of all composites are similar, and the size of alloy nanoparticles
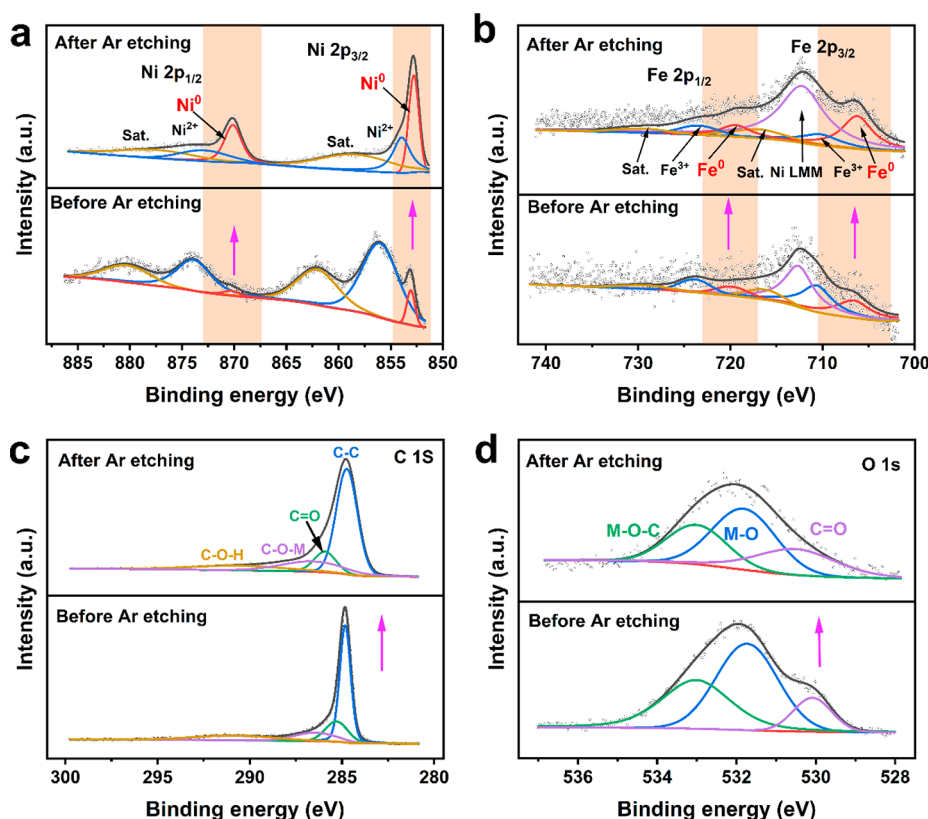
Figure 3. High-resolution spectra of $Ni_{SA}Fe_{SA}$-$Ni_{50}Fe$/CNT before and after argon etching: (a) Ni 2p; (b) Fe 2p; (c) C 1s; (d) O 1s.

is about 10 nm, which are uniformly distributed on the CNT wall (including the outer wall and the inner wall) with a high surface-coating rate. As shown in Figure 2c, CNTs are overlapped with each other to form a non-dense-packed conductive network, which is exceedingly conducive to the rapid migration of electrons. In addition, the pores between CNTs can be channels for gas emission during the catalysis process.[29] Furthermore, the small sizes of alloy particles are consistent with the broadening of the XRD diffraction peaks.

In addition, high angle annular dark field scanning transmission electron microscopy (HAADF-STEM) is used to confirm the single-atom distribution of $Ni_{SA}Fe_{SA}$-$Ni_{50}Fe$/CNT, the atom arrangement in the NiFe alloy, and the distribution of Ni, Fe, C, N, and O elements. As expected, abundant single atoms could be observed on the CNT wall in HAADF-STEM images (Figure 2d,e).[30] In addition, a linear scanning analysis is conducted to further prove the existence of single atoms (Figure 2f).[31] It can be seen that the intensities at the location of the bright spots (position 1 and 2 marked by yellow rectangles in Figure 2e) are significantly higher than those of the surrounding areas. Figure 2g gives the selected area electron diffraction (SAED) image of $Ni_{SA}Fe_{SA}$-$Ni_{50}Fe$/CNT. The radius of several bright diffraction rings in the illustration correspond to the plane spacings of C (003) and Ni (111), (200), and (220), respectively, which is also consistent with the XRD results. Figure 2h shows the Z-contrast image of $Ni_{SA}Fe_{SA}$-$Ni_{50}Fe$/CNT, which exhibits the atom arrangement of nanoalloys on CNTs. Although it is impossible to distinguish Ni and Fe because of the similar Z values of Ni ($Z = 28$) and Fe ($Z = 26$), the dislocation of atoms is immediately apparent.[32] As shown in Figure 2i, the atoms inside the alloy (position 3, marked by a red rectangle in

Figure 2h) are arranged neatly and orderly (the ordered atoms are represented by blue spheres), while the atoms at the junction of the alloy and CNT (position 4, marked by a blue rectangle in Figure 2h) are arranged chaotically (the disordered atoms are represented by green spheres). The disordered atom arrangement is caused by the bonding between nanoalloys and CNTs, indicating the strong interaction between nanoparticles and the carrier.

The energy dispersive spectrometer (EDS) mapping results are shown in Figure 2j, which provide the distribution details of Ni, Fe, C, N, and O elements in $Ni_{SA}Fe_{SA}$-$Ni_{50}Fe$/CNT. Ni and Fe are uniformly distributed in the nanoparticles, indicating that NiFe alloys are successfully obtained.[33] The proportion of Ni and Fe elements in the nanoparticles in Figure 2j is consistent with the result of inductively coupled plasma mass spectrometry (ICP-MS). It should be pointed out that the Ni/Fe ratio in the product (17/1) is lower than that of Ni/Fe in the salt solution (50/1). The possible reason is that the electronegativity of Fe^{3+} is higher than that of Ni^{2+}, so that Fe^{3+} could be preferably reduced in the preparation process.

The elemental compositions and valence states of the sample surface are analyzed by XPS. The XPS results of $Ni_{SA}Fe_{SA}$-$Ni_{50}Fe$/CNT both before and after argon etching are shown in Figure 3. Figure 3 gives the high-resolution XPS spectra of Ni 2p, Fe 2p, C 1s and O 1s. In the Ni 2p spectrum before argon etching (Figure 3a), the XPS peaks at 855.98 and 873.89 eV could be attributed to Ni^{2+} caused by the bonding between Ni and adsorbed oxygen. The peaks at 862.06 and 880.31 eV are the satellite peaks of Ni (denoted as Sat.).[34] In addition, two small peaks are observed at 853.06 and 870.24 eV, which correspond to Ni^0. After argon etching, Ni^0 becomes dominant, indicating that the interior of the nanoparticles is
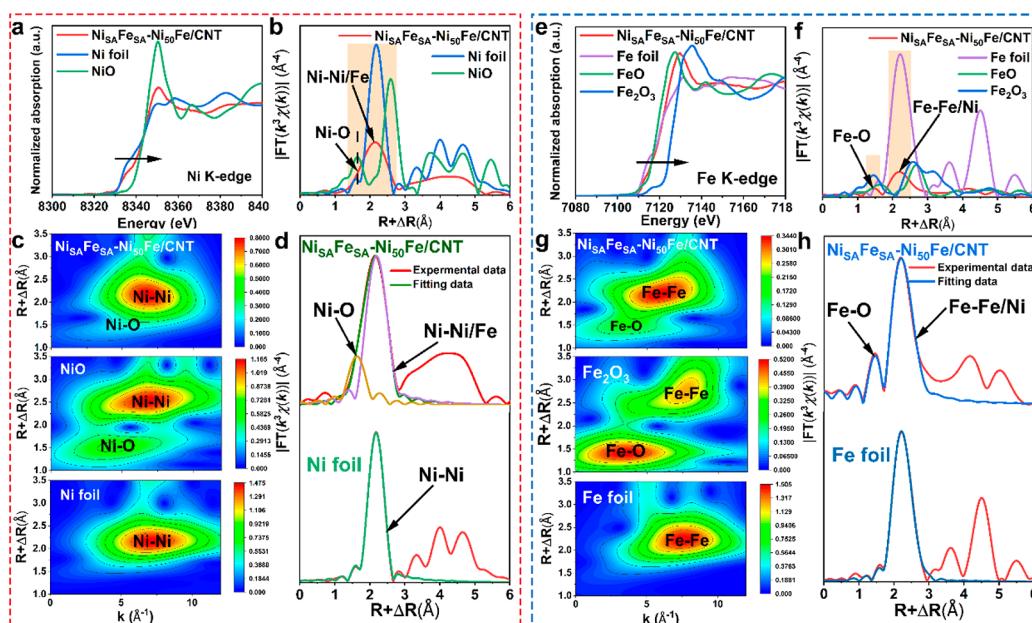
Figure 4. X-ray absorption spectra of Ni and Fe in $Ni_{SA}Fe_{SA}$-$Ni_{50}Fe/CNT$. (a) K-edge XANES of Ni (reference samples are Ni foil and NiO). (b) FT-EXAFS (without phase correction) of Ni. (c) WT-EXAFS of Ni. (d) Ni K-edge EXAFS fitting curve in R space. (e) K-edge XANES of Fe (reference samples are Fe foil, FeO, and Fe_2O_3). (f) FT-EXAFS (without phase correction) of Fe. (g) WT-EXAFS of Fe. (g) Fe K-edge EXAFS fitting curve in R space.

a metallic core. Similarly, in the high-resolution XPS spectrum of Fe 2p before argon etching, the metallic Fe^0 at 706.60 and 719.80 eV along with two XPS peaks at 710.60 and 723.80 eV are observed, which are ascribed to the bonding between Fe and O at the surface (Figure 3b).[30] The broad peak at around 712.56 eV can be attributed to the Auger peak of Auger Ni LMM. Moreover, the proportion of Fe^0 also increases after argon etching, suggesting that Fe is successfully reduced to a metallic core, which demonstrates that the core of nanoparticles is a highly conductive NiFe alloy. It should be noted that the intensity of XPS peaks in the Fe 2p spectrum is not as strong as that of Ni, which is caused by the low content of Fe doped in $Ni_{SA}Fe_{SA}$-$Ni_{50}Fe/CNT$. As shown in Figure 3c,d, the XPS spectra of O and C after argon etching do not obviously change in comparison to the spectra before etching. In the high-resolution spectrum of C 1s, the peaks at 284.81, 285.28, 286.43, and 292.82 eV correspond to C−C, C═O, C−O−M and C−O−H, respectively.[35,36] After argon etching, the peak of C−C is broadened, indicating the decreased strength, which is related to the peeling of CNT. In the high-resolution spectrum of O 1s, three peaks at 530.08, 531.73, and 533.02 eV are observed, which correspond to C═O, M−O, and M−O−C, respectively. Similarly, due to the peeling of CNT during argon etching, the peak of C═O becomes less obvious. The chemical bond of M−O−C, detected in both C 1s and O 1s spectra, can accelerate the electron transfer and improve the catalytic kinetic speed according to previous reports.[37]

In addition, the electronic structures and local coordination of Ni and Fe in $Ni_{SA}Fe_{SA}$-$Ni_{50}Fe/CNT$ are revealed by X-ray absorption near-edge structures (XANES) and extended X-ray absorption fine structures (EXAFS).[38] As shown in Figure 4a, the absorption edge of Ni in $Ni_{SA}Fe_{SA}$-$Ni_{50}Fe/CNT$ is higher than that of Ni foil (0), while lower than that of NiO (+2), indicating the oxidation state of Ni in the nanoparticles, which is consistent with the results of XPS.[39,40] As shown in Figure 4b, a significantly obvious broadened peak is observed in

Fourier-transformed EXAFS spectra (without phase correction) of Ni in $Ni_{SA}Fe_{SA}$-$Ni_{50}Fe/CNT$, which can be ascribed to a Ni−Ni/Fe bond at 2.15 Å and a Ni−O bond at 1.66 Å. In order to reveal the coordination situation of atoms more intuitively, the EXAFS result of Ni is transformed by a wavelet transform (WT-EXAFS), which can display the information on R space and K space simultaneously.[41] As shown in Figure 4c, both Ni−Ni/Fe and Ni−O are detected in the WT-EXAFS of Ni in $Ni_{SA}Fe_{SA}$-$Ni_{50}Fe/CNT$. Moreover, the fitting results also confirm that Ni atoms are coordinated with Ni/Fe and O (Figure 4d and Table S1). The signals of the Ni−Ni/Fe bond and Ni−O bond are also consistent with the XPS results, including the Ni−Ni detected in Ni 2p and M−O−C detected in C 1s and O 1s. In addition the Ni−O bond has a single-atom feature, which confirms the existence of single Ni atoms.

As shown in Figure 4e, the absorption edge of Fe in $Ni_{SA}Fe_{SA}$-$Ni_{50}Fe/CNT$ moves right in comparison with Fe foil, indicating the oxidation state of Fe. In addition, the absorption edge of Fe is almost same as that of FeO, so that the valence of Fe in $Ni_{SA}Fe_{SA}$-$Ni_{50}Fe/CNT$ is +2, which is also consistent the with XPS result of Fe 2p.[42] Similar to the case for Ni, both an Fe−O bond at 1.44 Å and an Fe−Fe/Ni bond at 2.20 Å are also found in the FT-EXAFS of Fe (without phase correction) (Figure 4f). The WT-EXAFS of Fe is shown in Figure 4g, and Fe−Fe/Ni and Fe−O bonds are also observed. Furthermore, the fitting results of Fe also confirmed that Fe atoms are coordinated with Fe/Ni and O (Figure 4h and Table S1). As was the case for Ni, the signals of the Fe−Fe/Ni bond and Fe−O bond are also consistent with the XPS results, including the Fe−Fe bond detected in the Fe 2p spectrum and M−O−C bond detected in C 1s and O 1s spectra. The Fe−O bond confirms the existence of single Fe atoms, as well.

The OER and HER catalytic performances of $Ni_{SA}Fe_{SA}$-Ni_xFe/CNT and $Ni_{SA}Co_{SA}$-Ni_xCo/CNT are tested in a common three-electrode system (see the Experimental Section for specific test parameters), and carbon cloth is used as the
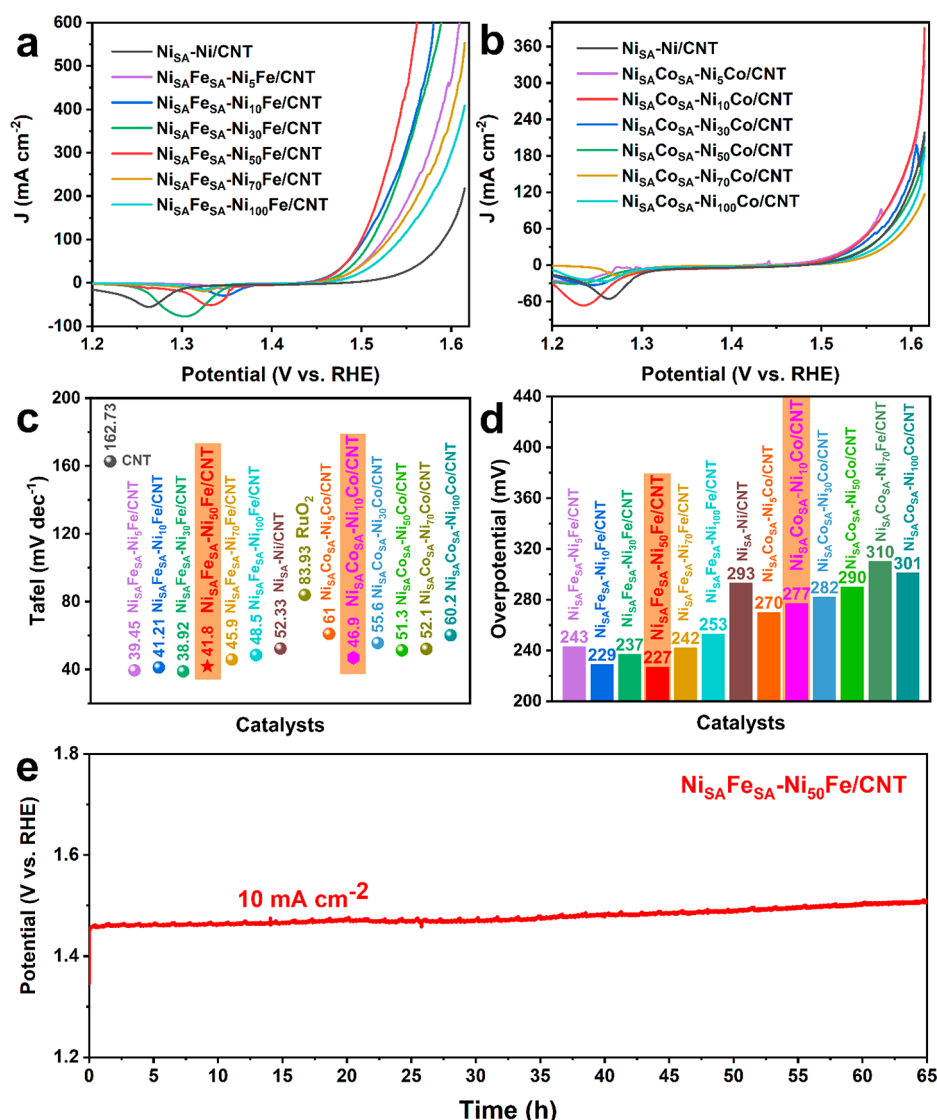
Figure 5. OER performances of $Ni_{SA}Fe_{SA}-Ni_xFe/CNT$ and $Ni_{SA}Co_{SA}-Ni_xCo/CNT$. (a) LSV curves of $Ni_{SA}Fe_{SA}-Ni_xFe/CNT$. (b) LSV curves of $Ni_{SA}Co_{SA}-Ni_xCo/CNT$. (c, d) Tafel slope comparison and overpotential comparison of $Ni_{SA}Fe_{SA}-Ni_xFe/CNT$ and $Ni_{SA}Co_{SA}-Ni_xCo/CNT$. (e) Chronopotentiometry (CP) curve of $Ni_{SA}Fe_{SA}-Ni_{50}Fe/CNT$ at 10 mA cm^{-2}.

carrier to support catalysts.[26] Before the catalytic performances of all samples are tested, the optimal loading is explored through $Ni_{SA}Fe_{SA}-Ni_{50}Fe/CNT$, and the result is shown in Figure S11. Optimized loading is used for all catalysts in subsequent tests. To avoid interference of determining the overpotential caused by huge oxidation peaks in the positive scanning process, the negative scanning from high voltage to low voltage is adopted in OER tests. Figure 5a–d shows the linear scanning curves of $Ni_{SA}Fe_{SA}-Ni_xFe/CNT$ and $Ni_{SA}Co_{SA}-Ni_xCo/CNT$ and comparisons of Tafel slopes and overpotentials to reach 10 mA cm^{-2}, respectively. Among all samples, the overpotential of $Ni_{SA}Fe_{SA}-Ni_{50}Fe/CNT$ to reach 10 mA cm^{-2} is the lowest, which is only 227 mV (Figure 5a,b,d). At a voltage of 1.56 V (vs the reversible hydrogen evolution potential, RHE), the current density of $Ni_{SA}Fe_{SA}-Ni_{50}Fe/CNT$ is as high as 600 mA cm^{-2} (Figure 5a), which surpasses those of many excellent OER catalysts reported so far.[43] The excellent OER properties of $Ni_{SA}Fe_{SA}-Ni_{50}Fe/CNT$, including ultralow overpotential and ultrahigh current density at low voltage, are ascribed to single atoms and fine nanoalloys

with a high surface loading rate on CNT and the synergistic effect between Ni and Fe. Doping the Fe element in Ni nanoparticles can help stabilize OER intermediates such as HO*, O*, and HOO*, which is beneficial for reducing the overpotential of the OER reaction.[44]

As shown in Figure 5c and Figure S12, both $Ni_{SA}Fe_{SA}-Ni_xFe/CNT$ and $Ni_{SA}Co_{SA}-Ni_xCo/CNT$ have small Tafel slopes, which are due to the unique heterostructure of composites, including the ultrathin NiFe and NiCo (oxy)-hydroxide layer generated on the surface of the bimetallic alloy, the conductive alloy core, and the non-dense-packed network structure. The Tafel slope of $Ni_{SA}Fe_{SA}-Ni_{50}Fe/CNT$ is only 41.8 mV dec^{-1}, revealing its enhanced electron and mass transfer ability. On an evaluation of the OER performance from overpotentials and current density, both $Ni_{SA}Fe_{SA}-Ni_xFe/CNT$ and $Ni_{SA}Co_{SA}-Ni_xCo/CNT$ show a "volcanic" trend. This "volcanic" trend is consistent with our DFT-based calculation results (Figure S16). Fe and Co could enhance the adsorption/desorption capacity of intermediate products, and there is a great influence of different doping ratios on the
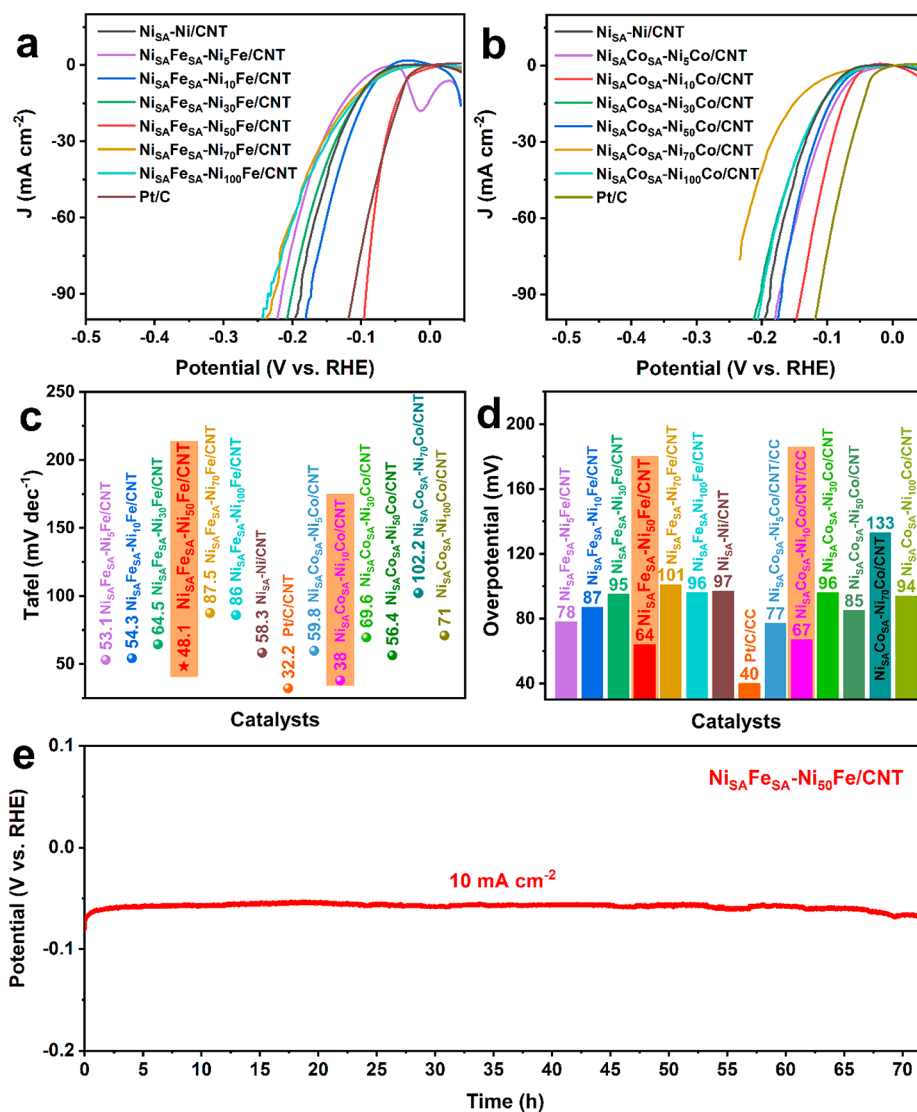
Figure 6. HER performances of $Ni_{SA}Fe_{SA}$-Ni_xFe/CNT and $Ni_{SA}Co_{SA}$-Ni_xCo/CNT. (a) LSV curves of $Ni_{SA}Fe_{SA}$-Ni_xFe/CNT. (b) LSV curves of $Ni_{SA}Co_{SA}$-Ni_xCo/CNT. (c, d) Tafel slope comparison and overpotential comparison of $Ni_{SA}Fe_{SA}$-Ni_xFe/CNT and $Ni_{SA}Co_{SA}$-Ni_xCo/CNT. (e) Chronopotentiometry (CP) curve of $Ni_{SA}Fe_{SA}$-$Ni_{50}Fe/CNT$ at 10 mA cm^{-2}.

active layer. Only when the adsorption and desorption abilities reach a balance will the performance be on "the volcano top".

Electrochemical stability is another key index to evaluate the catalytic performance. The chronopotentiometry (CP) of $Ni_{SA}Fe_{SA}$-$Ni_{50}Fe/CNT$ at 10 mA cm^{-2} is measured, and the result is shown in Figure 5e. In 1 M KOH, the voltage of $Ni_{SA}Fe_{SA}$-$Ni_{50}Fe/CNT$ increases only slightly after 65 h, suggesting its excellent catalytic stability. The durable ability of $Ni_{SA}Fe_{SA}$-$Ni_{50}Fe/CNT$ for OER catalysis contradicts that in previous studies. For example, Liu et al. proved that NiFe hydroxide would gradually dissolve in the process of the OER, which resulted in its poor cycling stability.[45] It is possible that NiFe and NiCo (oxy)hydroxides will reconstruct *in situ* on the surface of the alloy in $Ni_{SA}Fe_{SA}$-$Ni_{50}Fe/CNT$ even if they are dissolved during the catalytic process, which would lead to excellent catalytic stability for $Ni_{SA}Fe_{SA}$-$Ni_{50}Fe/CNT$.[46] Such an *in situ* generation mechanism demonstrates its better adaptability in comparison to directly prepared (oxy)-hydroxides for the OER.

$Ni_{SA}Fe_{SA}$-Ni_xFe/CNT and $Ni_{SA}Co_{SA}$-Ni_xCo/CNT also show excellent HER catalytic performance. As shown in Figure 6,

both $Ni_{SA}Fe_{SA}$-Ni_xFe/CNT and $Ni_{SA}Co_{SA}$-Ni_xCo/CNT show a good promotion effect on HER catalysis. Among the two series of $Ni_{SA}Fe_{SA}$-Ni_xFe/CNT and $Ni_{SA}Co_{SA}$-Ni_xCo/CNT, the catalysts with the best HER catalytic performance are $Ni_{SA}Fe_{SA}$-$Ni_{50}Fe/CNT$ and $Ni_{SA}Co_{SA}$-$Ni_{10}Co/CNT$, respectively. The required overpotentials for the two catalysts to achieve a current density of 10 mA cm^{-2} are only 64 and 67 mV, respectively, which are very close to that of the commercial Pt/C electrode of 40 mV (Figure 6a,b,d). As seen from Figure 6c and Figure S15, the Tafel slopes of $Ni_{SA}Fe_{SA}$-$Ni_{50}Fe/CNT$, $Ni_{SA}Co_{SA}$-$Ni_{10}Co/CNT$, and Pt/C are 48.1, 38.0, and 32.2 mV dec^{-1}, respectively, which are significantly lower than those of other materials with different Ni/Fe and Ni/CO ratios. The outstanding HER properties of $Ni_{SA}Fe_{SA}$-$Ni_{50}Fe/CNT$ and $Ni_{SA}Co_{SA}$-$Ni_{10}Co/CNT$ can be partially attributed to the promoted electron migration ability enhanced by cross-carrying CNT network carriers. Figure 6e shows the CP curves of $Ni_{SA}Fe_{SA}$-$Ni_{50}Fe/CNT$ measured at a current density of 10 mA cm^{-2}. $Ni_{SA}Fe_{SA}$-$Ni_{50}Fe/CNT$ also shows a brilliant electrochemical stability for the HER, and the stable time is as long as 72 h.

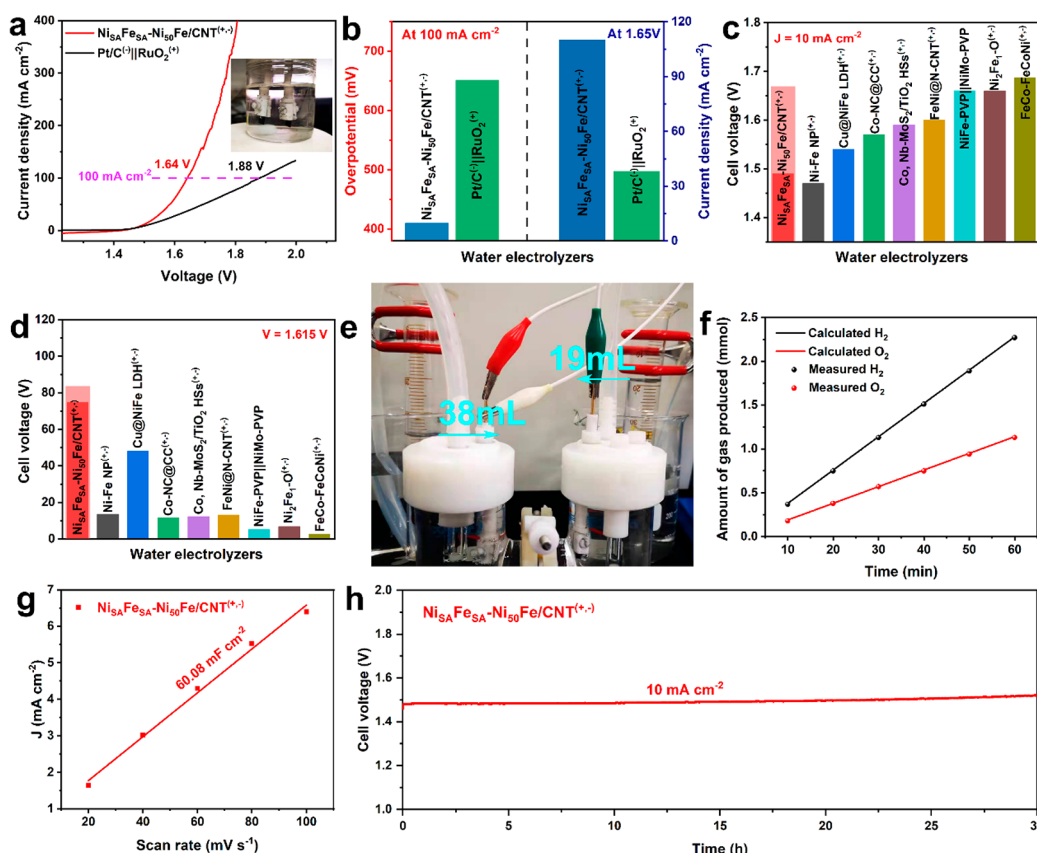**Figure 7.** Overall water splitting. (a) Comparison of $Ni_{SA}Fe_{SA}-Ni_{50}Fe/CNT^{(+,-)}$ and $Pt/C^{(-)}||RuO_2^{(+)}$ for overall water splitting activities at 1 M KOH. The illustration is a device diagram for overall water splitting. (b) Overpotential comparison of achieving 10 mA cm^{-2} and current density comparison at 1.65 V of $Ni_{SA}Fe_{SA}-Ni_{50}Fe/CNT^{(+,-)}$ and $Pt/C^{(-)}||RuO_2^{(+)}$. (c) Comparison of the cell voltages to achieve 10 mA cm^{-2} among different water alkaline electrolyzers. (d) Comparison of the current densities of these electrolyzers at 1.615 V in 1 M KOH. (e) Photo of the electrocatalytic device for testing the volumes of hydrogen and oxygen generated by $Ni_{SA}Fe_{SA}-Ni_{50}Fe/CNT^{(+,-)}$ for water splitting by a drainage method. (f) Comparison of the theoretical calculation and the actual amounts of gas produced by $Ni_{SA}Fe_{SA}-Ni_{50}Fe/CNT^{(+,-)}$ at a current density of 500 mA cm^{-2}. (g, h) Electrochemical active area and CP curves, respectively, of $Ni_{SA}Fe_{SA}-Ni_{50}Fe/CNT^{(+,-)}$ at 10 mA cm^{-2}.

Next, a water electrolyzer is assembled with $Ni_{SA}Fe_{SA}-Ni_{50}Fe/CNT$ as both anode and cathode simultaneously. A photo of the two-electrode system water electrolyzer is shown in the inset of Figure 7a. The performance for electrocatalytic overall water splitting is also tested in 1 M KOH. For comparison, the electrocatalytic overall water splitting performance of the electrolyzer with Pt/C as the anode and RuO_2 as the cathode is also tested under the same conditions. Figure 7a gives a comparison of the LSV curves (negative scanning) of $Ni_{SA}Fe_{SA}-Ni_{50}Fe/CNT^{(+,-)}$ and $Pt/C^{(-)}||RuO_2^{(+)}$, which illustrates that the electrocatalytic overall water splitting performance of $Ni_{SA}Fe_{SA}-Ni_{50}Fe/CNT^{(+,-)}$ is much better than that of noble-metal-based $Pt/C^{(-)}||RuO_2^{(+)}$. The overpotentials to reach 10 and 100 mA cm^{-2} required for $Ni_{SA}Fe_{SA}-Ni_{50}Fe/CNT^{(+,-)}$ are only 260 and 410 mV, respectively, which are lower than the 279 mV (10 mA cm^{-2}) and 650 mV (100 mA cm^{-2}) of $Pt/C^{(-)}||RuO_2^{(+)}$ (Figure 7a,b). At 1.65 V, the current density of $Ni_{SA}Fe_{SA}-Ni_{50}Fe/CNT^{(+,-)}$ is 110 mA cm^{-2}, which is much higher than that of $Pt/C^{(-)}||RuO_2^{(+)}$ (39 mA cm^{-2}). In addition, at a cell voltage of 1.80 V, the current density of $Ni_{SA}Fe_{SA}-Ni_{50}Fe/CNT^{(+,-)}$ is as high as 382 mA cm^{-2}, which is around 5 times higher than that of $Pt/C^{(-)}||RuO_2^{(+)}$ (77 mA cm^{-2}). A low overpotential (260 mV) and ultrahigh current density at low cell voltage have rarely been reported in the previous literature. In addition to commercial catalysts, other electrocatalytic catalysts for water splitting reported in recent

years are also summarized, including the required voltage to reach 10 mA cm^{-2} (Figure 7c and Table S2) and the current density at 1.615 V (Figure 7d). As can be seen, among these catalysts, $Ni_{SA}Fe_{SA}-Ni_{50}Fe/CNT^{(+,-)}$ and Ni-Fe NP$^{(+,-)}$ show the lowest overpotential of 260 and 240 mV, respectively. However, the current density of Ni-Fe NP$^{(+,-)}$ (14 mA cm^{-2}) is much lower than that of $Ni_{SA}Fe_{SA}-Ni_{50}Fe/CNT^{(+,-)}$ (75 mA cm^{-2}) at 1.615 V. From these comparisons, we can see that the prepared $Ni_{SA}Fe_{SA}-Ni_{50}Fe/CNT^{(+,-)}$ is one of the best catalysts for electrolytic overall water splitting.

The device shown in Figure 7e is assembled to test the volume of hydrogen and oxygen generated by $Ni_{SA}Fe_{SA}-Ni_{50}Fe/CNT^{(+,-)}$ at 500 mA cm^{-2} in 1 M KOH. The picture taken during the catalytic process shows that the amount of produced hydrogen is about 38 mL and the amount of oxygen is half of the volume of hydrogen, about 19 mL. Figure 7f shows the amounts of hydrogen and oxygen produced by theoretical calculations and actual measurement. The actual amounts are roughly the same as those of the theoretical calculations, which suggests that $Ni_{SA}Fe_{SA}-Ni_{50}Fe/CNT^{(+,-)}$ has an ultrahigh Faraday efficiency. In addition, an electrical chemical capacitance measurement method is used to estimate the $Ni_{SA}Fe_{SA}-Ni_{50}Fe/CNT^{(+,-)}$ electrochemical area (60.08 mF cm^{-2}), which is much higher than those of previously reported materials (Figure 7g and Figure S18). The superhigh electrochemical active areas are beneficial to improving the
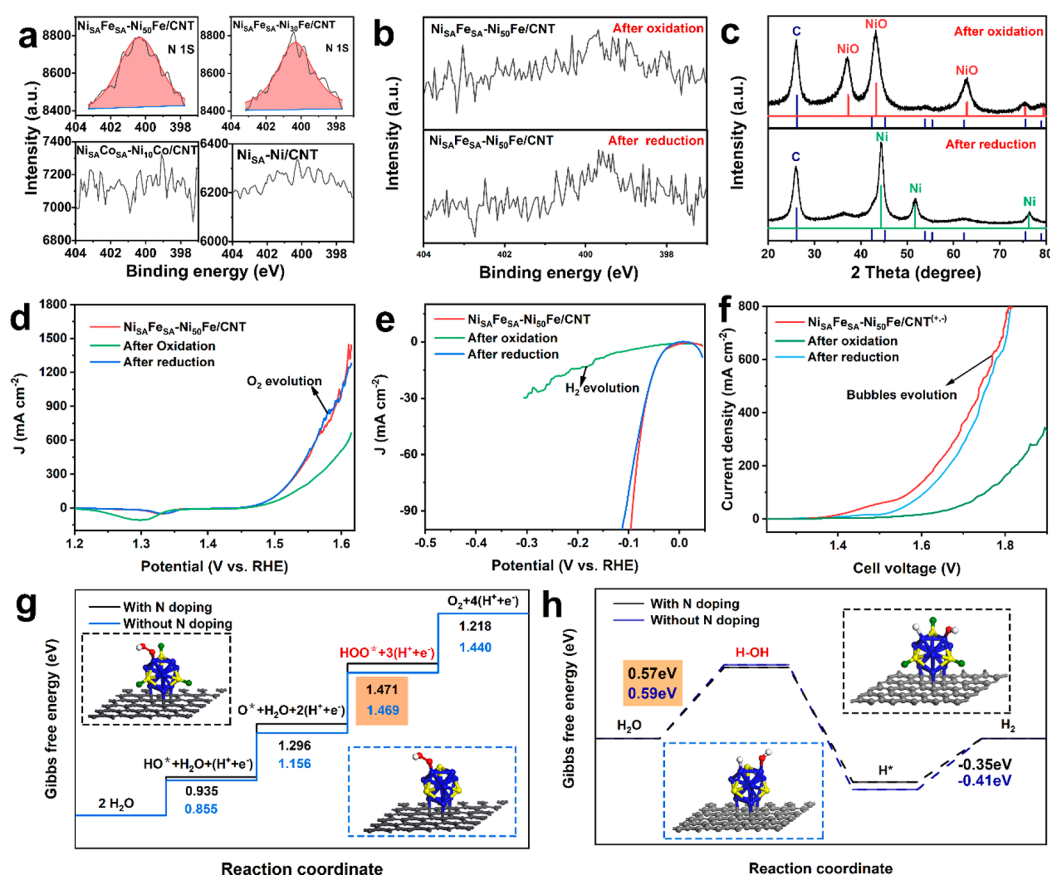
Figure 8. (a) Comparison of high-resolution N spectra of $Ni_{SA}Fe_{SA}$-$Ni_{50}Fe/CNT$, $Ni_{SA}Fe_{SA}$-$Ni_{30}Fe/CNT$, Ni_{SA}-Ni/CNT, and $Ni_{SA}Co_{SA}$-$Ni_{10}Co/CNT$. (b) Comparison of high-resolution N spectra of $Ni_{SA}Fe_{SA}$-$Ni_{50}Fe/CNT$ after oxidation in air and rereduction in H_2/Ar. (c) XRD diffraction patterns of $Ni_{SA}Fe_{SA}$-$Ni_{50}Fe/CNT$ after oxidation in air and rereduction in H_2/Ar. (d−f) OER, HER, and overall water splitting catalytic performance comparisons, respectively, of $Ni_{SA}Fe_{SA}$-$Ni_{50}Fe/CNT$ and $Ni_{SA}Fe_{SA}$-$Ni_{50}Fe/CNT$ after oxidation in air and reduction in H_2/Ar. (g, h) OER Gibbs free energy diagrams and HER Gibbs free energy diagrams of $Ni_{SA}Fe_{SA}$-$Ni_{50}Fe/CNT$ with or without N doping. The insets give the schematic diagrams of the models. The black balls represent C atoms, the blue balls represent Ni atoms, the yellow balls represent Fe atoms, the green balls represent N atoms, the red balls represent O atoms, and the white balls represent H atoms.

catalytic performance of overall water splitting. Moreover, the catalytic stability of $Ni_{SA}Fe_{SA}$-$Ni_{50}Fe/CNT^{(+,-)}$ for electrocatalytic overall water splitting is tested (Figure 7h) at 10 mA cm^{-2}, and the electrolyzer is stable for over 30 h. In conclusion, $Ni_{SA}Fe_{SA}$-$Ni_{50}Fe/CNT$ is one of the most excellent supermaterials for overall water splitting and has a bright future for greatly improving the industrial production efficiency of electrocatalytic overall water splitting.

The high-resolution diagram of N 1s provides evidence that an obvious N element coordination exists in the prepared Fe-doped samples, while no XPS peak of the N element is observed in Ni_{SA}-Ni/CNT and $Ni_{SA}Co_{SA}$-Ni_xCo/CNT, which suggests that Fe is the N-doped site (Figure 8a). In order to analyze the effect of the nitrogen element on catalytic performance, a simple two-step oxidation and rereduction procedure is employed to remove N coordination. Specifically, the $Ni_{SA}Fe_{SA}$-$Ni_{50}Fe/CNT$ sample is fully oxidized at 400 °C in air and then rereduced in an H_2/Ar mixture. As shown in Figure 8b, an N peak is not observed in either the oxidized or rereduced catalysts, indicating that the N doping in the original catalyst is successfully removed. The XRD results show that Ni is fully oxidized to NiO after being kept in the air at 400 °C and reduced to Ni after is heated in the H_2/Ar mixture at 400 °C for 2 h (Figure 8c). After this two-step process, the morphology of the sample is still the same (Figure S19). Under

the same electrochemical conditions, the oxidized and rereduced catalysts are tested to obtain their OER, HER, and overall water splitting performances (Figure 8d−f). After oxidation, the performance of the sample decreases significantly, especially for the HER performance. The reason is that an oxidized core would lead to increased resistance and slow the electron migration, and thus the barrier required for the catalytic reactions increases. It is amazing that the performances of OER, HER, and overall water splitting of the rereduction sample recover completely to their original levels.

In addition to the experimental verification, a DFT-based theoretical calculation is also carried out by introducing a nanocluster based on the Woolf structure.[47] The Gibbs free energies of each OER and HER reaction step are calculated and shown in Figure 8g,h and Figure S16. These results show that the thermodynamic barriers of the rate-determining step are almost identical for the samples with and without N doping. It is confirmed that nitrogen element coordination does not affect the catalytic performance in our system. More importantly, the above results indicate that the effective structure of the catalyst could be completely reconstructed by a simple two-step process, which will increase the adaptability of catalyst in practical applications and provide the possibility of catalyst reactivation.

CONCLUSION

In summary, $Ni_{SA}Fe_{SA}$-Ni_xFe/CNT and $Ni_{SA}Co_{SA}$-Ni_xCo/CNT with single atoms and nanoalloys simultaneously supported on CNTs are successfully prepared, which can be used for efficient OER, HER, and overall water splitting catalysis under alkaline conditions. Due to a series of advantages, including the synergistic catalysis of single atoms and nanoalloys, ultrahigh electrochemical active areas, strong electron transfer ability, and effective gas release, the optimized $Ni_{SA}Fe_{SA}$-$Ni_{50}Fe$/CNT catalyst can provide a current density of 10 mA cm^{-2} for the OER and HER at ultralow overpotentials of 227 and 64 mV and can be stable for 65 h and 72 h, respectively. In addition, an alkaline water electrolyzer with $Ni_{SA}Fe_{SA}$-$Ni_{50}Fe$/CNT as both the cathode and anode also exhibits excellent electrocatalytic performance for overall water splitting. When the current densities are 10 and 100 mA cm^{-2}, the overpotentials are only 260 and 410 mV, respectively. At a cell voltage of 1.80 V, the current density of $Ni_{SA}Fe_{SA}$-$Ni_{50}Fe$/CNT$^{(+,-)}$ is as high as 382 mA cm^{-2}, which surpasses those of most materials reported so far. Furthermore, the experimental results and DFT-based theoretical calculations confirm that nitrogen element coordination does not affect the catalytic performance in the optimized $Ni_{SA}Fe_{SA}$-$Ni_{50}Fe$/CNT system and the effective structure of the catalyst can be completely reconstructed by a simple two-step process. This work reveals that the non-noble-metal bifunctional catalyst achieves extremely excellent electrocatalytic performance for the OER, HER, and overall water splitting, which shows a great potential for economically realizing industrialized overall water splitting.

EXPERIMENTAL SECTION

Chemicals Used. Carbon nanotubes (CNT) were obtained from Beijing Deke Daojin Technology Co., Ltd. Nickel nitrate $(Ni(NO_3)_2 \cdot 6H_2O$, 98%) was purchased from Guangdong Guanghua Technology Co., Ltd. Ferric nitrate $(Fe(NO_3)_3 \cdot 9H_2O$, 98.5%), cobaltous nitrate $(Co(NO_3)_2 \cdot 6H_2O$, 98.5%), potassium hydroxide (KOH, 85%), and absolute ethanol $(C_2H_5OH$, 99.7%) were obtained from China National Pharmaceutical Group Corporation. Sodium borohydride (NaBH$_4$, 96%) was purchased from Kermel Chemical Reagent Company. Ruthenium(IV) oxide (RuO$_2$, 99.9%), platinum on graphitized carbon (20 wt %, Pt/C), and Nafion solution (5 wt %) were obtained from Sigma-Aldrich. The electrodes, including the counter electrode and reference electrode, were purchased from Shanghai Chenhua Instrument Company, and the carbon cloth was obtained from Taiwan carbon energy technology company. All reagents were analytical grade and were used without further purification. The argon/hydrogen (90/10) gas mixture (Ar/H$_2$, 99%) was used as received.

Synthesis of Ni$_{SA}$-Ni/CNT. Ni$_{SA}$-Ni/CNT was synthesized by a chemical reduction and heat treatment. First, nickel nitrate was dispersed in deionized water to prepare 40 mL of a 0.015 M solution. Next, 0.02 g of acid-treated CNTs (treated with aqua regia at 120 °C for 3 h) was added into the salt solution and then vacuum pumping (1000 r/min for 5 min), ultrasonic dispersion (30 min), and stirring (20 min) were conducted to obtain a completely dispersed, homogeneous mixed solution containing Ni^{2+} and CNT. Subsequently, 40 mL of a 0.015 M NaBH$_4$ solution was prepared. After that, the NaBH$_4$ solution was pumped into the mixed solution at a rate

of 350 μL/min through a peristaltic pump. After aging for 20 h in the environment of ice bath and under the condition of continuous stirring, the solution was vacuum-filtered and dried to obtain the precursor (40 °C, 24 h). Lastly, the precursor was kept in a hydrogen/argon mixed atmosphere at 400 °C for 2 h to prepare Ni$_{SA}$-Ni/CNT.

Synthesis of Ni$_{SA}$Fe$_{SA}$-Ni$_x$Fe/CNT and Ni$_{SA}$Co$_{SA}$-Ni$_x$Co/CNT. Ni$_{SA}$Fe$_{SA}$-Ni$_x$Fe/CNT and Ni$_{SA}$Co$_{SA}$-Ni$_x$Co/CNT were synthesized by the same method. Different from Ni$_{SA}$-Ni$_x$/CNT, Ni^{2+} and Fe^{3+} or Ni^{2+} and Co^{2+} should be contained in a salt solution for Ni$_{SA}$Fe$_{SA}$-Ni$_x$Fe/CNT and Ni$_{SA}$Co$_{SA}$-Ni$_x$Co/CNT, respectively. The ratio of Ni^{2+} to Fe^{3+} or of Ni^{2+} to Co^{2+} was x, which is consistent with the metal proportion in the sample name. With Ni$_{SA}$Fe$_{SA}$-Ni$_{50}$Fe/CNT as an example, the specific preparation process was as follows. First, ferric nitrate and nickel nitrate (the Ni^{2+}/Fe^{3+} molar ratio was 50) were dispersed in deionized water to prepare 40 mL of a 0.015 M solution. Next, 0.02 g of acid-treated CNTs was added into the salt solution and then vacuum pumping, ultrasonic dispersion, and stirring were conducted. Subsequently, 40 mL of 0.015 M NaBH$_4$ solution was pumped into the mixed solution at a rate of 350 μL/min through a peristaltic pump. After aging for 20 h in the environment of an ice bath and under the condition of continuous stirring, the solution was vacuum-filtered and dried to obtain the precursor. Finally, the precursor was kept in a hydrogen/argon mixed atmosphere at 400 °C for 2 h to prepare Ni$_{SA}$Fe$_{SA}$-Ni$_{50}$Fe/CNT.

Materials Characterization. The phase identification of the prepared catalysts was studied by X-ray diffraction (SmartLab 3 kW, Rigaku Corporation, working voltage 40 kV) with Cu Kα radiation (at a diffraction angle ranging from 10 to 80° and a scan rate of 8°/min). The morphologies of catalysts were characterized by field emission scanning electron microscopy (Nova NanoSEM230, FEI Electron Optics BV) and transmission electron microscopy (JEM-2100F, Rigaku Corporation). Spherical aberration corrected transmission electron microscopy (Themis Z G2 60-300, Thermo Fisher) was employed to characterize the microstructures and the distribution of single atoms and different elements in Ni$_{SA}$Fe$_{SA}$-Ni$_{50}$Fe/CNT. The X-ray photoelectron spectra (XPS) before and after argon etching were obtained with Al Kα radiation (ESCALAB250Xi, Thermo Fisher-VG Scientific) to collect element compositions and valence states of the sample surface (technical support provided by www.eceshi.com). The X-ray absorption spectra (XAS), including XANES and EXAFS, were collected on the beamline BL07A1 at the NSRRC (technical support provided by Ceshigo Research Service, www.ceshigo.com). The radiation was monochromated by a Si (111) double-crystal monochromator. XANES and EXAFS data analysis were processed by Athena software and then further deconvoluted by the wavelet transform (WT) method.

Electrochemical Tests. The electrochemical tests for the OER and HER were conducted by CHI760E electrochemical workstation in a three-electrode system, with Hg/HgO as the reference electrode, a platinum sheet as the counter electrode, and carbon cloth loaded with catalysts as the working electrode. The electrolyte was 1 M KOH. The specific preparation method of the carbon cloth working electrode was as fpllows. The optimized loading of the carbon cloth working electrode was first explored; 5.0, 10.0, and 20.0 mg of Ni$_{SA}$Fe$_{SA}$-Ni$_{50}$Fe/CNT were dispersed in a mixed solution cintaining 960 μL of ethanol and 40 μL of 5% Nafion solution and then were sonicated for 2 h. Subsequently, 50 μL of

catalyst ink was dropped on a 0.25 cm^2 carbon cloth and the electrode was dried at room temperature. After the exploration for optimized loading, the working electrodes of other catalysts (Ni$_{SA}$-Ni/CNT, Ni$_{SA}$Fe$_{SA}$-Ni$_x$Fe/CNT, Ni$_{SA}$Co$_{SA}$-Ni$_x$Co/CNT, and 20% Pt/C) were prepared on the basis of the optimal mass loading of 2 mg cm^{-2} on carbon cloth.

The scanning rate of the polarization curve for the OER and HER was 5 mV s^{-1}. All of the LSV tests were represented with *iR* compensation, which was done via the *iR* compensation command in CHI software by applying the test potential, step amplitude, compensation leve,l and overshoot level as 0 V, 0.05 V, 95%, and 2%, respectively. Chronopotentiometric measurements were performed to evaluate the long-term stability. The determination of ECSA was calculated by measuring the CV curves at different scan rates (20, 40, 60, 80, and 100 mV s^{-1}).

The water splitting electrolyzer was assembled with Ni$_{SA}$Fe$_{SA}$-Ni$_{50}$Fe/CNT as both cathode and anode materials. The scanning rate of the polarization curve for water splitting was 5 mV s^{-1}. The chronopotentiometric measurement was performed to evaluate the long-term stability. The volumes of hydrogen and oxygen produced were measured by the drainage method at a current density of 500 mA cm^{-2} under the standard conditions (25 °C, 1 atm). The volumes of oxygen and hydrogen collected every 10 min were recorded.

DFT Calculations. The DFT calculation work in this paper was carried out through the Vienna ab initio software package (VASP). The planar projection enhanced wave (PAW) method was used to describe the interaction between valence electrons and core electronic effects. The generalized gradient approximation (GGA) of Perdew–Burke–Ernzerhof (PBE) was used for the exchange and correlation energy. The plane wave cutoff energy iswas set to 500 eV. In order to simulate the loading of nanoscale NiFe particles on the surface of CNTs, a 13-atom nanocluster (Ni$_x$Fe$_{13-x}$) was chosen. On the basis of the Woolf structure, the face-centered cubic nickel metal was more inclined to the cubic octahedral geometric structure, and Ni$_{13}$ was the smallest of the octahedral "magic numbers".[48,49] Since the size of the CNT in the experiment is larger than that of NiFe nanoparticles, some studies have shown that the curvature of the carbon nanotube carrier has little effect. Therefore, the carbon nanotube carrier is wasapproximated as a graphene sheet to reduce the complexity of the model. The model added a 15 Å vacuum layer along the Z axis to eliminate the interaction between the upper and lower surfaces. The model uses a Monkhorst *K*-point grid with a 5 × 5 × 1 grid. All geometric optimizations were performed using the conjugate gradient algorithm implemented in VASP. The convergence conditions of force and energy are 0.01 and 1.0 × 10^{-5} eV Å^{-1}, respectively.

In order to be the closest to the actual situation, Ni$_{SA}$Fe$_{SA}$-Ni$_{50}$Fe/CNT with the best performance was taken as the research object and the Ni$_{10}$Fe$_3$/CNT with the lowest overpotential was selected as the calculation model among the Ni$_x$Fe$_{13-x}$/CNT systems. The OER Gibbs free energies of each step for Ni$_{10}$Fe$_3$-N/CNT with N doping and Ni$_{10}$Fe$_3$/CNT showed that the rate-determining steps of Ni$_{10}$Fe$_3$-N/CNT with N doping and Ni$_{10}$Fe$_3$/CNT without N doping are the same, both of which are the third step. The thermodynamic barriers of the rate-determining step were almost identical, which were 1.471 eV for the Ni$_{10}$Fe$_3$-N/CNT and 1.469 eV for the Ni$_{10}$Fe$_3$/CNT, respectively. Moreover, the HER kinetics of Ni$_{10}$Fe$_3$-N/CNT and Ni$_{10}$Fe$_3$/CNT exhibited the same rate-determining step and similar activated water adsorption

energies (ΔG_{H-OH} of Ni$_{10}$Fe$_3$-N/CNT was 0.57 eV and ΔG_{H-OH} of Ni$_{10}$Fe$_3$/CNT was 0.57 eV). In short, through experimental investigations and DFT calculations, it was confirmed that N doping was not the main reason for the catalytic performance difference of the OER, HER, and electrocatalytic water splitting between Ni$_{SA}$Fe$_{SA}$-Ni$_x$Fe/CNT and Ni$_{SA}$Co$_{SA}$-Ni$_x$Co/CNT in our systems.

■ ASSOCIATED CONTENT

ⓢ Supporting Information

The Supporting Information is available free of charge at https://pubs.acs.org/doi/10.1021/acscatal.1c04454.

> XRD patterns, TEM images, HADDF-STEM images, and OER and HER performance of Ni$_{SA}$Fe$_{SA}$-Ni$_x$Fe/CNT and Ni$_{SA}$Co$_{SA}$-Ni$_x$Co/CNT, exploration result of the optimal load, schematic diagram of the free energy model and overpotential volcanic patterns, CV curves of the Ni$_{SA}$Fe$_{SA}$-Ni$_{50}$Fe/CNT$^{(+,-)}$ electrolyzer, and a comparison of the overall water-splitting activities among different earth-abundant electrocatalysts (PDF)

■ AUTHOR INFORMATION

Corresponding Authors

Shen Gong – *State Key Laboratory of Powder Metallurgy, School of Materials Science and Engineering, Central South University, Changsha 410083, People's Republic of China;* ⓞ orcid.org/0000-0003-2520-7406; Email: gongshen011@csu.edu.cn

Xueping Gan – *State Key Laboratory of Powder Metallurgy, School of Materials Science and Engineering, Central South University, Changsha 410083, People's Republic of China;* Email: ganxueping@csu.edu.cn

Zhou Li – *State Key Laboratory of Powder Metallurgy, School of Materials Science and Engineering, Central South University, Changsha 410083, People's Republic of China;* Email: lizhou6931@csu.edu.cn

Authors

Wenhui Luo – *State Key Laboratory of Powder Metallurgy, School of Materials Science and Engineering, Central South University, Changsha 410083, People's Republic of China*

Yang Wang – *State Key Laboratory of Powder Metallurgy, School of Materials Science and Engineering, Central South University, Changsha 410083, People's Republic of China*

Liuxiong Luo – *State Key Laboratory of Powder Metallurgy, School of Materials Science and Engineering, Central South University, Changsha 410083, People's Republic of China*

Mengni Wei – *State Key Laboratory of Powder Metallurgy, School of Materials Science and Engineering, Central South University, Changsha 410083, People's Republic of China*

Yixuan Li – *State Key Laboratory of Powder Metallurgy, School of Materials Science and Engineering, Central South University, Changsha 410083, People's Republic of China*

Yuyuan Zhao – *School of Engineering, University of Liverpool, Liverpool L69 3GH, U.K.;* ⓞ orcid.org/0000-0003-2356-8435

Zhenghong Zhu – *Department of Mechanical Engineering, York University, Toronto M3J 1P3, Canada*

Complete contact information is available at: https://pubs.acs.org/10.1021/acscatal.1c04454

■ REFERENCES

(1) Liang, C.; Zou, P.; Nairan, A.; Zhang, Y.; Liu, J.; Liu, K.; Hu, S.; Kang, F.; Fan, H. J.; Yang, C. Exceptional performance of hierarchical Ni−Fe oxyhydroxide@NiFe alloy nanowire array electrocatalysts for large current density water splitting. *Energy Environ. Sci.* **2020**, *13* (1), 86−95.

(2) Li, C.; Zhang, Z.; Liu, R. In Situ Growth of 3D NiFe LDH-POM Micro-Flowers on Nickel Foam for Overall Water Splitting. *Small* **2020**, *16* (46), 2003777.

(3) Wu, P.; Wu, J.; Si, H.; Zhang, Z.; Liao, Q.; Wang, X.; Dai, F.; Ammarah, K.; Kang, Z.; Zhang, Y. 3D Holey-Graphene Architecture Expedites Ion Transport Kinetics to Push the OER Performance. *Adv. Energy Mater.* **2020**, *10* (22), 2001005.

(4) Liu, D.; Ai, H.; Li, J.; Fang, M.; Chen, M.; Liu, D.; Du, X.; Zhou, P.; Li, F.; Lo, K. H.; Tang, Y.; Chen, S.; Wang, L.; Xing, G.; Pan, H. Surface Reconstruction and Phase Transition on Vanadium−Cobalt−Iron Trimetal Nitrides to Form Active Oxyhydroxide for Enhanced Electrocatalytic Water Oxidation. *Adv. Energy Mater.* **2020**, *10* (45), 2002464.

(5) Wang, J.; Xu, F.; Jin, H.; Chen, Y.; Wang, Y. Non-Noble Metal-based Carbon Composites in Hydrogen Evolution Reaction: Fundamentals to Applications. *Adv. Mater.* **2017**, *29* (14), 1605838.

(6) Zhao, Y.; Gao, Y.; Chen, Z.; Li, Z.; Ma, T.; Wu, Z.; Wang, L. Trifle Pt coupled with NiFe hydroxide synthesized via corrosion engineering to boost the cleavage of water molecule for alkaline water-splitting. *Appl. Catal., B* **2021**, *297*, 120395.

(7) Suryanto, B. H. R.; Wang, Y.; Hocking, R. K.; Adamson, W.; Zhao, C. Overall electrochemical splitting of water at the heterogeneous interface of nickel and iron oxide. *Nat. Commun.* **2019**, *10* (1), 5599.

(8) Goor-Dar, M.; Travitsky, N.; Peled, E. Study of hydrogen redox reactions on platinum nanoparticles in concentrated HBr solutions. *J. Power Sources* **2012**, *197*, 111−115.

(9) Wang, P.; Zhu, J.; Pu, Z.; Qin, R.; Zhang, C.; Chen, D.; Liu, Q.; Wu, D.; Li, W.; Liu, S.; Xiao, J.; Mu, S. Interfacial engineering of Co nanoparticles/Co₂C nanowires boosts overall water splitting kinetics. *Appl. Catal., B* **2021**, *296*, 120334.

(10) Dai, L.; Chen, Z. N.; Li, L.; Yin, P.; Liu, Z.; Zhang, H. Ultrathin Ni(0)-Embedded Ni(OH)₂ Heterostructured Nanosheets with Enhanced Electrochemical Overall Water Splitting. *Adv. Mater.* **2020**, *32* (8), 1906915.

(11) Wang, Y.; Li, X.; Zhang, M.; Zhou, Y.; Rao, D.; Zhong, C.; Zhang, J.; Han, X.; Hu, W.; Zhang, Y.; Zaghib, K.; Wang, Y.; Deng, Y. Lattice-Strain Engineering of Homogeneous NiS₀.₅Se₀.₅ Core-Shell Nanostructure as a Highly Efficient and Robust Electrocatalyst for Overall Water Splitting. *Adv. Mater.* **2020**, *32* (40), 2000231.

(12) Roy, S.; Bagchi, D.; Dheer, L.; Sarma, S. C.; Rajaji, V.; Narayana, C.; Waghmare, U. V.; Peter, S. C. Mechanistic insights into the promotional effect of Ni substitution in non-noble metal carbides for highly enhanced water splitting. *Appl. Catal., B* **2021**, *298*, 120560.

(13) Zhang, L.; Zhu, Y.; Nie, Z.; Li, Z.; Ye, Y.; Li, L.; Hong, J.; Bi, Z.; Zhou, Y.; Hu, G. Co/MoC Nanoparticles Embedded in Carbon Nanoboxes as Robust Trifunctional Electrocatalysts for a Zn-Air Battery and Water Electrocatalysis. *ACS Nano* **2021**, *15*, 13399−13414.

(14) Riyajuddin, S.; Azmi, K.; Pahuja, M.; Kumar, S.; Maruyama, T.; Bera, C.; Ghosh, K. Super-Hydrophilic Hierarchical Ni-Foam-Graphene-Carbon Nanotubes-Ni₂P-CuP₂ Nano-Architecture as Efficient Electrocatalyst for Overall Water Splitting. *ACS Nano* **2021**, *15* (3), 5586−5599.

(15) Guo, Y.; Tang, J.; Henzie, J.; Jiang, B.; Xia, W.; Chen, T.; Bando, Y.; Kang, Y. M.; Hossain, M. S. A.; Sugahara, Y.; Yamauchi, Y. Mesoporous Iron-doped MoS₂/CoMo₂S₄ Heterostructures through Organic-Metal Cooperative Interactions on Spherical Micelles for Electrochemical Water Splitting. *ACS Nano* **2020**, *14* (4), 4141−4152.

(16) Tsounis, C.; Lu, X.; Bedford, N. M.; Subhash, B.; Thomsen, L.; Zhang, Q.; Ma, Z.; Ostrikov, K. K.; Bendavid, A.; Scott, J. A.; Amal, R.; Han, Z. Valence Alignment of Mixed Ni-Fe Hydroxide Electrocatalysts through Preferential Templating on Graphene Edges for Enhanced Oxygen Evolution. *ACS Nano* **2020**, *14* (9), 11327−11340.

(17) Peng, Y.; Lu, B.; Chen, S. Carbon-Supported Single Atom Catalysts for Electrochemical Energy Conversion and Storage. *Adv. Mater.* **2018**, *30*, 1801995.

(18) Li, Z.; Wang, Z.; Xi, S.; Zhao, X.; Sun, T.; Li, J.; Yu, W.; Xu, H.; Herng, T. S.; Hai, X.; Lyu, P.; Zhao, M.; Pennycook, S. J.; Ding, J.; Xiao, H.; Lu, J. Tuning the Spin Density of Cobalt Single-Atom Catalysts for Efficient Oxygen Evolution. *ACS Nano* **2021**, *15* (4), 7105−7113.

(19) Feng, C.; Faheem, M. B.; Fu, J.; Xiao, Y.; Li, C.; Li, Y. Fe-Based Electrocatalysts for Oxygen Evolution Reaction: Progress and Perspectives. *ACS Catal.* **2020**, *10* (7), 4019−4047.

(20) Xu, Z.; Zhang, X.; Wang, X.; Fang, J.; Zhang, Y.; Liu, X.; Zhu, W.; Yan, Y.; Zhuang, Z. Synthesis of Ag-Ni-Fe-P Multielemental Nanoparticles as Bifunctional Oxygen Reduction/Evolution Reaction Electrocatalysts. *ACS Nano* **2021**, *15* (4), 7131−7138.

(21) Ortiz Pena, N.; Ihiawakrim, D.; Han, M.; Lassalle-Kaiser, B.; Carenco, S.; Sanchez, C.; Laberty-Robert, C.; Portehault, D.; Ersen, O. Morphological and Structural Evolution of Co₃O₄ Nanoparticles Revealed by in Situ Electrochemical Transmission Electron Microscopy during Electrocatalytic Water Oxidation. *ACS Nano* **2019**, *13* (10), 11372−11381.

(22) Yoon, K. R.; Hwang, C. K.; Kim, S. H.; Jung, J. W.; Chae, J. E.; Kim, J.; Lee, K. A.; Lim, A.; Cho, S. H.; Singh, J. P.; Kim, J. M.; Shin, K.; Moon, B. M.; Park, H. S.; Kim, H. J.; Chae, K. H.; Ham, H. C.; Kim, I. D.; Kim, J. Y. Hierarchically Assembled Cobalt Oxynitride Nanorods and N-Doped Carbon Nanofibers for Efficient Bifunctional Oxygen Electrocatalysis with Exceptional Regenerative Efficiency. *ACS Nano* **2021**, *15*, 11218−11230.

(23) Peng, M.; Shi, D.; Sun, Y.; Cheng, J.; Zhao, B.; Xie, Y.; Zhang, J.; Guo, W.; Jia, Z.; Liang, Z.; Jiang, L. 3D Printed Mechanically Robust Graphene/CNT Electrodes for Highly Efficient Overall Water Splitting. *Adv. Mater.* **2020**, *32* (23), 1908201.

(24) Dong, C.; Kou, T.; Gao, H.; Peng, Z.; Zhang, Z. Eutectic-Derived Mesoporous Ni-Fe-O Nanowire Network Catalyzing Oxygen Evolution and Overall Water Splitting. *Adv. Energy Mater.* **2018**, *8* (5), 1701347.

(25) Tao, Z.; Wang, T.; Wang, X.; Zheng, J.; Li, X. MOF-Derived Noble Metal Free Catalysts for Electrochemical Water Splitting. *ACS Appl. Mater. Interfaces* **2016**, *8* (51), 35390−35397.

(26) Zhang, Y.; Xia, X.; Cao, X.; Zhang, B.; Tiep, N. H.; He, H.; Chen, S.; Huang, Y.; Fan, H. J. Ultrafine Metal Nanoparticles/N-Doped Porous Carbon Hybrids Coated on Carbon Fibers as Flexible and Binder-Free Water Splitting Catalysts. *Adv. Energy Mater.* **2017**, *7* (15), 1700220.

(27) Lei, H.; Wang, Z.; Yang, F.; Huang, X.; Liu, J.; Liang, Y.; Xie, J.; Javed, M. S.; Lu, X.; Tan, S.; Mai, W. NiFe nanoparticles embedded N-doped carbon nanotubes as high-efficient electrocatalysts for wearable solid-state Zn-air batteries. *Nano Energy* **2020**, *68*, 104293.

(28) Liu, P.; Chen, B.; Liang, C.; Yao, W.; Cui, Y.; Hu, S.; Zou, P.; Zhang, H.; Fan, H. J.; Yang, C. Tip-Enhanced Electric Field: A New

Mechanism Promoting Mass Transfer in Oxygen Evolution Reactions. *Adv. Mater.* **2021**, *33* (9), 2007377.

(29) Fu, G.; Yan, X.; Chen, Y.; Xu, L.; Sun, D.; Lee, J. M.; Tang, Y. Boosting Bifunctional Oxygen Electrocatalysis with 3D Graphene Aerogel-Supported Ni/MnO Particles. *Adv. Mater.* **2018**, *30* (5), 1704609.

(30) Lee, J.; Kumar, A.; Yang, T.; Liu, X.; Jadhav, A. R.; Park, G. H.; Hwang, Y.; Yu, J.; Nguyen, C. T. K.; Liu, Y.; Ajmal, S.; Kim, M. G.; Lee, H. Stabilizing the OOH* intermediate via pre-adsorbed surface oxygen of a single Ru atom-bimetallic alloy for ultralow overpotential oxygen generation. *Energy Environ. Sci.* **2020**, *13* (12), 5152−5164.

(31) Zhao, C. X.; Liu, J. N.; Wang, J.; Ren, D.; Yu, J.; Chen, X.; Li, B. Q.; Zhang, Q. A DeltaE = 0.63 V Bifunctional Oxygen Electrocatalyst Enables High-Rate and Long-Cycling Zinc-Air Batteries. *Adv. Mater.* **2021**, *33* (15), 2008606.

(32) Kim, D.; Xie, C.; Becknell, N.; Yu, Y.; Karamad, M.; Chan, K.; Crumlin, E. J.; Norskov, J. K.; Yang, P. Electrochemical Activation of CO_2 through Atomic Ordering Transformations of AuCu Nanoparticles. *J. Am. Chem. Soc.* **2017**, *139* (24), 8329−8336.

(33) Ren, W.; Tan, X.; Qu, J.; Li, S.; Li, J.; Liu, X.; Ringer, S. P.; Cairney, J. M.; Wang, K.; Smith, S. C.; Zhao, C. Isolated copper-tin atomic interfaces tuning electrocatalytic CO_2 conversion. *Nat. Commun.* **2021**, *12* (1), 1449.

(34) Huang, Y.; Zhang, S. L.; Lu, X. F.; Wu, Z. P.; Luan, D.; Lou, X. W. D. Trimetallic Spinel $NiCo_{2-x}Fe_xO_4$ Nanoboxes for Highly Efficient Electrocatalytic Oxygen. *Evolution. Angew. Chem., Int. Ed.* **2021**, *60* (21), 11841−11846.

(35) Yang, L.; Loh, L.; Nandakumar, D. K.; Lu, W.; Gao, M.; Wee, X. L. C.; Zeng, K.; Bosman, M.; Tan, S. C. Sustainable Fuel Production from Ambient Moisture via Ferroelectrically Driven MoS_2 Nanosheets. *Adv. Mater.* **2020**, *32* (25), 2000971.

(36) Wang, Q.; Xue, X.; Lei, Y.; Wang, Y.; Feng, Y.; Xiong, X.; Wang, D.; Li, Y. Engineering of Electronic States on Co_3O_4 Ultrathin Nanosheets by Cation Substitution and Anion Vacancies for Oxygen Evolution Reaction. *Small* **2020**, *16* (24), 2001571.

(37) Zhong, X.; Huang, K.; Zhang, Y.; Wang, Y.; Feng, S. Constructed Interfacial Oxygen-Bridge Chemical Bonding in Core-Shell Transition Metal Phosphides/Carbon Hybrid Boosting Oxygen Evolution Reaction. *ChemSusChem* **2021**, *14* (10), 2188−2197.

(38) Zhang, Z.; Zhao, X.; Xi, S.; Zhang, L.; Chen, Z.; Zeng, Z.; Huang, M.; Yang, H.; Liu, B.; Pennycook, S. J.; Chen, P. Atomically Dispersed Cobalt Trifunctional Electrocatalysts with Tailored Coordination Environment for Flexible Rechargeable Zn−Air Battery and Self-Driven Water Splitting. *Adv. Energy Mater.* **2020**, *10* (48), 2002896.

(39) Zhao, G.; Li, P.; Cheng, N.; Dou, S. X.; Sun, W. An Ir/ $Ni(OH)_2$ Heterostructured Electrocatalyst for the Oxygen Evolution Reaction: Breaking the Scaling Relation, Stabilizing Iridium(V), and Beyond. *Adv. Mater.* **2020**, *32* (24), 2000872.

(40) Zhang, X.; Zhang, S.; Yang, Y.; Wang, L.; Mu, Z.; Zhu, H.; Zhu, X.; Xing, H.; Xia, H.; Huang, B.; Li, J.; Guo, S.; Wang, E. A General Method for Transition Metal Single Atoms Anchored on Honeycomb-Like Nitrogen-Doped Carbon Nanosheets. *Adv. Mater.* **2020**, *32*, 1906905.

(41) Cheng, X.; Lu, Y.; Zheng, L.; Pupucevski, M.; Li, H.; Chen, G.; Sun, S.; Wu, G. Engineering local coordination environment of atomically dispersed platinum catalyst via lattice distortion of support for efficient hydrogen evolution reaction. *Mater. Today Energy* **2021**, *20*, 100653.

(42) Chala, S. A.; Tsai, M. C.; Su, W. N.; Ibrahim, K. B.; Thirumalraj, B.; Chan, T. S.; Lee, J. F.; Dai, H.; Hwang, B. J. Hierarchical 3D Architectured Ag Nanowires Shelled with NiMn-Layered Double Hydroxide as an Efficient Bifunctional Oxygen Electrocatalyst. *ACS Nano* **2020**, *14*, 1770−1782.

(43) Wang, T.; Nam, G.; Jin, Y.; Wang, X.; Ren, P.; Kim, M. G.; Liang, J.; Wen, X.; Jang, H.; Han, J.; Huang, Y.; Li, Q.; Cho, J. NiFe(Oxy) Hydroxides Derived from NiFe Disulfides as an Efficient Oxygen Evolution Catalyst for Rechargeable Zn-Air Batteries: The Effect of Surface S Residues. *Adv. Mater.* **2018**, *30* (27), 1800757.

(44) Yu, L.; Zhou, H.; Sun, J.; Qin, F.; Yu, F.; Bao, J.; Yu, Y.; Chen, S.; Ren, Z. Cu nanowires shelled with NiFe layered double hydroxide nanosheets as bifunctional electrocatalysts for overall water splitting. *Energy Environ. Sci.* **2017**, *10* (8), 1820−1827.

(45) Chen, R.; Hung, S. F.; Zhou, D.; Gao, J.; Yang, C.; Tao, H.; Yang, H. B.; Zhang, L.; Zhang, L.; Xiong, Q.; Chen, H. M.; Liu, B. Layered Structure Causes Bulk NiFe Layered Double Hydroxide Unstable in Alkaline Oxygen Evolution Reaction. *Adv. Mater.* **2019**, *31* (41), 1903909.

(46) Zhang, B.; Wang, L.; Cao, Z.; Kozlov, S. M.; García de Arquer, F. P.; Dinh, C. T.; Li, J.; Wang, Z.; Zheng, X.; Zhang, L.; Wen, Y.; Voznyy, O.; Comin, R.; De Luna, P.; Regier, T.; Bi, W.; Alp, E. E.; Pao, C.-W.; Zheng, L.; Hu, Y.; Ji, Y.; Li, Y.; Zhang, Y.; Cavallo, L.; Peng, H.; Sargent, E. H. High-valence metals improve oxygen evolution reaction performance by modulating 3d metal oxidation cycle energetics. *Nat. Catal.* **2020**, *3* (12), 985−992.

(47) Fu, W.; Wang, Y.; Zhang, H.; He, M.; Fang, L.; Yang, X.; Huang, Z.; Li, J.; Gu, X.; Wang, Y. Epitaxial growth of graphene on V_8C_7 nanomeshs for highly efficient and stable hydrogen evolution reaction. *J. Catal.* **2019**, *369*, 47−53.

(48) Popov, V. N. Curvature effects on the structural, electronic and optical properties of isolated single-walled carbon nanotubes within a symmetry-adapted non-orthogonal tight-binding model. *New J. Phys.* **2004**, *6*, 17−17.

(49) Miehle, W.; Kandler, O.; Leisner, T.; Echt, O. Mass spectrometric evidence for icosahedral structure in large rare gas clusters: Ar, Kr, Xe. *J. Chem.Phys.* **1989**, *91* (10), 5940−5952.